

Research



Article submitted to journal

Subject Areas:

astrophysics, solar physics

Keywords:Elemental Composition, Solar
Coronal Dynamics, Solar Activity**Author for correspondence:**

David Long

e-mail: david.long@dcu.ieComparing First Ionisation
Potential bias diagnostics in
the solar atmosphereK. D. Spruksta¹, D. M. Long^{1,2}, A. S. H. To³¹Centre for Astrophysics and Relativity, School of
Physical Sciences, Dublin City University²Astronomy & Astrophysics Section, Dublin Institute for
Advanced Studies, Dublin D02 XF86, Ireland³European Space Agency (ESA), European Space
Research and Technology Centre (ESTEC),
Keplerlaan 1, 2201 AZ Noordwijk, The Netherlands

Plasma composition in the solar atmosphere differs between the photosphere and corona, producing an observable difference in elemental abundance known as the FIP effect. The FIP effect is characterised by the ratio of low to high FIP elements, giving a number known as the FIP bias. FIP bias values vary between different regions of the solar atmosphere, with typical observed values of ~ 1 for coronal holes, ~ 1.5 - 2 for the quiet Sun, and ~ 3 for active regions. The Extreme ultraviolet Imaging Spectrometer (EIS) onboard the *Hinode* spacecraft has enabled the widespread use of the Si X/S X line pair as a FIP bias diagnostic, but EIS observes other line pairs that can be used to estimate FIP bias. We consider three FIP bias diagnostics observed by *Hinode*/EIS (Si X/S X, Ca XIV/Ar XIV, and Fe XVI/S XIII), comparing the FIP bias between Quiet Sun and an Active region. We also assume a range of signal-to-noise (SNR) cutoff values for each pixel, finding that while the SNR cutoff affects the number of useable pixels, higher (lower) SNR cutoffs remove (retain) a tail of high FIP bias values within the measured distribution. However, the median value of the FIP bias distribution remains largely unchanged. These results show the importance of a more nuanced view of FIP bias when using this vitally important diagnostic rather than a simplistic one-size-fits-all approach.

1. Introduction

Analysis of spectroscopic observations of the solar atmosphere have revealed a distinct and measureable difference in elemental abundance between the solar photosphere and corona. This difference is particularly identifiable between the abundances of elements of high (≥ 10 eV) and low (< 10 eV) first ionisation potential (FIP), and is commonly referred to as the FIP bias [1, 2]. Once imprinted in a given region of the solar atmosphere the FIP bias generally remains conserved, although processes such as plasma mixing or gravitational settling can cause changes in plasma composition. Overall, this general conservation makes FIP bias a very useful diagnostic for identifying the origin of e.g., solar wind plasma [3], and has enabled the connection science promulgated by the ESA/NASA *Solar Orbiter* spacecraft [4].

The process by which plasma is fractionated in the solar atmosphere remains the subject of intense research, with the leading theory suggesting that waves in coronal loops induce a ponderomotive force at the loop footpoints in the interface region between the solar photosphere and corona. This ponderomotive force then acts on ions that are largely low-FIP, transporting them upward into the corona and leaving the largely neutral high-FIP elements behind, thus producing the observed FIP bias [cf. 5]. Previous observations have identified signatures in the photosphere of the waves predicted to induce a ponderomotive associated with coronal signatures of enhanced FIP bias [e.g., 6–9]. However, although there have been some indications of chromospheric and transition region signatures of related processes [cf. 10, 11], no direct observations have yet been made of the fractionation process.

Previous work, particularly using the spatially resolved observations provided by the Extreme ultraviolet Imaging Spectrometer [EIS; 12] onboard the *Hinode* spacecraft [13] has shown that different regions of the solar atmosphere have different FIP bias, with some correlation found between increasing magnetic field strength and FIP bias [14–18]. This is also consistent with historical observations using spectroheliograms from *Skylab* [19]. The FIP bias of the solar atmosphere is therefore a powerful plasma diagnostic that has been identified as a possible tracer of plasma evolution through the solar atmosphere [5]. As a result, the *Solar Orbiter* spacecraft has been designed to include two instruments that can measure FIP bias using remote-sensing (the SPectral Imaging of the Coronal Environment, SPICE, spectrometer [20]), and *in-situ* (the Solar Wind Analyser, SWA, particle detector [21]) measurements.

However, although all of these instruments measure FIP bias using a combination of high- and low-FIP elements, the combinations of elements are different in each case, sensitive to different temperatures and ionisation fraction in the chromosphere. Previous work has also tended to assume single values for FIP bias measurements of different regions of the solar atmosphere. The cores of active regions are widely assumed to have FIP bias values of ~ 3 [22], while the quiet Sun has a typical FIP bias of ~ 1.5 – 2 [16, 23]. Ensuring that the widely used FIP bias diagnostics behave in a manner consistent with their temperature sensitivities in different regions of the solar atmosphere [14–18], and provide interpretable FIP bias values of those different regions, is therefore vital for our understanding of this increasingly important parameter.

Here we compare three commonly used FIP bias diagnostics from the *Hinode*/EIS instrument, namely the Si X/S X, Fe XVI/S XIII, and Ca XIV/Ar XIV line ratios, focussing on how they behave in distinct regions of the solar atmosphere. Using a full-disk mosaic taken between 18–20 October 2015, we identified a region of Quiet Sun and an Active region and compared the distribution of FIP bias values in those regions for each diagnostic studied. The observations and data are presented in Section 2, with the results outlined in Section 3, before some conclusions are drawn in Section 4.

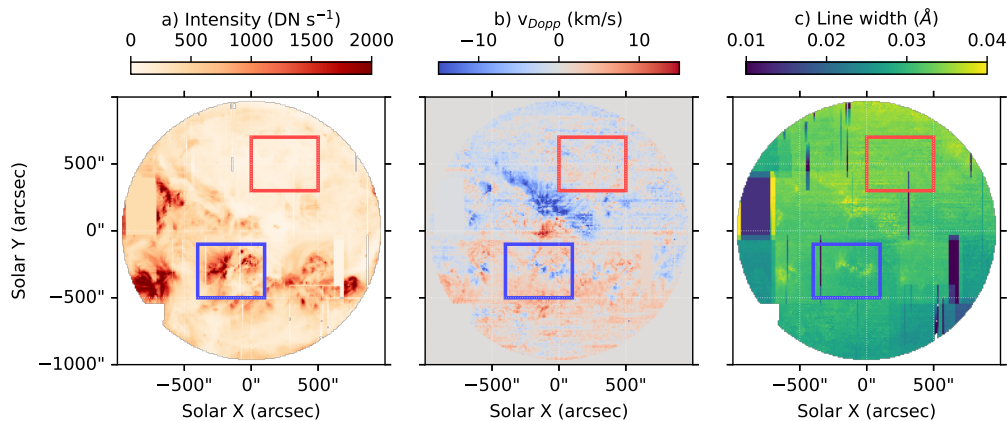


Figure 1. Full disk mosaics taken from 18–20 Oct 2015 by *Hinode*/EIS showing the fitted peak intensity (panel a), Doppler velocity (panel b), and line width (panel c) of the Fe XII 195.119 Å emission line. The red (blue) box shows the Quiet Sun (active region) region of interest further examined in Section 3.

2. Observations

The set of raster scans comprising the full disk observations described here were taken by the Extreme ultraviolet Imaging Spectrometer [EIS; 12] onboard the *Hinode* spacecraft [13] from 18–20 October 2015. *Hinode*/EIS regularly takes full-disk mosaic scans of the solar corona across a range of Extreme UltraViolet (EUV) lines, enabling multiple research opportunities including a comparison to be made between active regions of different ages [cf. 17], and the first full disk FIP maps [14]. Figure 1 shows the peak fitted intensity (left panel), Doppler velocity (middle panel) and nonthermal velocity (right panel) of the Fe XII 195.119 Å emission line for this full disk raster mosaic. It is clear from Figure 1 that the solar disk at the time included a number of active regions and a large region of quiet Sun, enabling a direct comparison to be made between the different FIP bias diagnostics measured here in these different regions.

The full-disk mosaics used here were produced using a series of 26 pointings of the *Hinode* spacecraft taken between 10:27:19 UT on 18-October-2015 and 00:26:12 UT on 20-October-2015, in each case using the DHB_007 EIS study. This produces 123 pointings per raster, with a 4" step using the 2" slit, taking observations in 25 spectral windows. Each of the individual EIS rasters were processed and fitted using the *eispac* python package [24], with the fitted spectral lines then used to calculate the elemental abundance using several different diagnostics. The most commonly used FIP bias diagnostic produced by this full disk spectral scan is the low-FIP Si X 258.37 Å/intermediate-FIP S X 264.23 Å diagnostic previously used by [14] to probe the origin of the slow solar wind. However, this study also contains the spectral lines required to produce the low-FIP Ca XIV 193.87 Å/high-FIP Ar XIV 194.40 Å and the low-FIP Fe XVI 262.98 Å/intermediate-FIP S XIII 256.69 Å FIP bias diagnostics [25].

We used the Markov Chain Monte Carlo technique developed by [14] and previously outlined in detail by [17, 26] to process the individual EIS rasters and produce the full-disk Si X/S X FIP bias map¹. This approach fits spectral lines from consecutive ionisation stages of Fe VIII - Fe XVII using either single or multiple Gaussians as appropriate. Note that typically single Gaussians are used unless the line is blended. These lines have formation temperatures in the range ~ 0.5 – 5.5 MK, and the combination of fitted line intensities can then be used to calculate the differential emission measure, and estimate the FIP bias assuming an electron density estimated using the Fe XIII 202.04 Å/203.83 Å line ratio. This diagnostic is most sensitive to plasma with a temperature of

¹Code available at https://github.com/andyto1234/demcmc_FIP

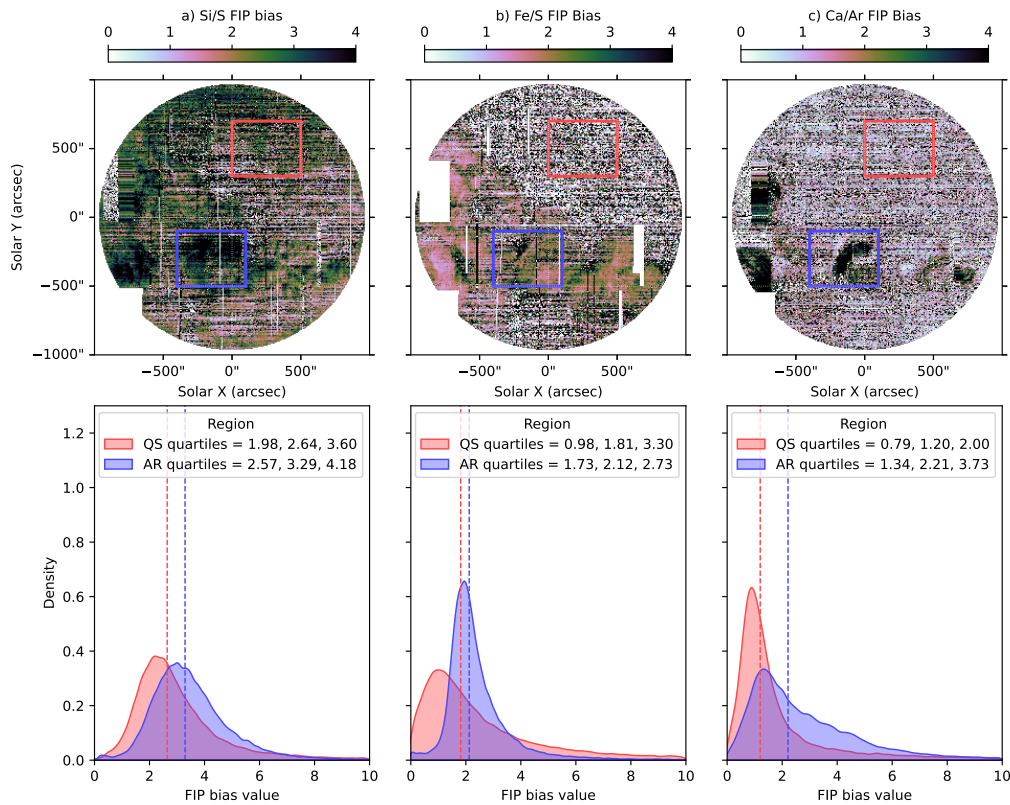


Figure 2. Top row: Full disk mosaics taken by *Hinode*/EIS showing the derived Si X/S X (panel a, left), Fe XVI/S XIII (panel b, centre), and Ca XIV/Ar XIV (panel c, right) FIP maps. The red (blue) box shows the Quiet Sun (active region) region of interest. Bottom row shows the corresponding Kernel Density Estimator (KDE) plots of the distributions corresponding to the Quiet Sun (red) and active region (blue) from the derived Si X/S X (left), Fe XVI/S XIII (centre), and Ca XIV/Ar XIV (right) FIP maps. The legend gives the 25th, 50th (i.e., median), and 75th percentile values for each distribution

$T \sim 1\text{--}2$ MK, corresponding to quiet Sun and quiescent active regions. Note that this analysis was done using version 10 of the CHIANTI database [27, 28] assuming the photospheric abundances of [29, 30] and *Hinode*/EIS calibration of [31]. The result of this derivation is shown in panel a of Figure 2. It is clear from Figure 2a that the active regions have higher FIP bias values of ~ 4 .

The second diagnostic, Ca XIV/Ar XIV, was used to probe slightly higher temperature plasma. The Ca XIV and Ar XIV lines have a higher formation temperature of ~ 3.5 MK, corresponding to the hot cores of active regions. In contrast to the full DEM approach used to derive the Si X/S X diagnostic, the Ca XIV/Ar XIV diagnostic was derived by first fitting the individual spectral lines and then taking their ratio following the example of [32] who note that variations in the elemental abundances of the two elements primarily affect the magnitude of their contribution functions rather than their shape as a function of temperature. As a result, the intensity ratio can be used to derive the relative abundance between Ca and Ar [see also 33–35, for further discussions]. For this diagnostic, shown in Figure 2c, a clear distinction can be made between the hotter active regions and the cooler quiet Sun. The hotter active regions display a higher FIP bias value of ~ 4 , with the cooler quiet Sun regions exhibiting a lower FIP bias value of ≤ 1 , with the image shown in Figure 2c indicating that a lot of the pixels have FIP bias values of 0 that are ignored in this analysis.

The final diagnostic examined here was the Fe XVI/S XIII diagnostic described and previously used by [36, 37]. The Fe XVI and S XIII lines were first fitted using single Gaussians as they are unblended, with the FIP bias calculated using the MCMC approach also used to estimate the Si X/S X diagnostic. This process is described in more detail in [36, 37]. The Fe XVI and S XIII lines are sensitive to plasma at $T \sim 2\text{--}3$ MK, with the resulting full disk mosaic shown in Figure 2b. Figure 2b shows stronger signal in the different active regions, with the quiet Sun regions showing a lot more white pixels. This indicates that the Fe XVI/S XIII diagnostic is sensitive to active region and surrounding plasma, with a FIP bias of $\sim 2\text{--}3$ observed for the different active regions in contrast to the FIP bias of ≤ 1 seen for quiet Sun regions, again indicating that a lot of the pixels have FIP bias values of 0 that are ignored in this analysis (as for the Ca XIV/Ar XIV diagnostic above).

3. Results

(a) Comparing different regions of the solar atmosphere

To further investigate the different FIP bias diagnostics and better understand the importance of temperature and density sensitivity on the distribution of FIP bias values we defined two regions of interest for a more detailed examination. The red boxes in Figures 1 and 2 highlight a region of Quiet Sun, while the blue boxes highlight an active region. We then used a kernel density estimation (KDE) approach to compare the distribution of FIP bias values in the different regions [cf. 10, 38, 39]. This approach does not require the use of user-defined bins [40], and enables a clear identification of the different feature of the individual datasets. It is clear from each of the three panels in the bottom row of Figure 2 that as expected there is a difference in FIP bias between the regions defined as Quiet Sun and Active Region. For each diagnostic studied, the distribution corresponding to the Quiet Sun (shown in red) tends to peak at a lower FIP bias value than the distribution corresponding to the Active Region (shown in blue). This is to be expected, with the quiet Sun typically expected to exhibit a FIP bias value of $\sim 1.5\text{--}2$, corresponding to weakly fractionated photospheric plasma [16]. However, there is a clear distribution of values for the Quiet Sun region as measured using each diagnostic, with a strong tail of values having a value greater than 2 for each diagnostic, but particularly both the Si X/S X and Fe XVI/S XIII diagnostics. The quartile values of the distributions are also given in the legends, with Quiet Sun median (i.e., 50th percentile) values of 2.64 (Si X/S X), 1.20 (Ca XIV/Ar XIV), and 1.81 (Fe XVI/S XIII).

While active regions are considered to have higher FIP bias values of ~ 3 [22], the distributions shown in Figure 2 are quite broad, with tails extending to FIP bias values of ~ 10 . It is interesting that the 25th to 75th percentiles of the Si X/S X distribution (containing 50% of the values of the distribution) extend from $\sim 2.57\text{--}4.18$, with a median value of 3.29. The Ca XIV/Ar XIV diagnostic also shows a distribution of FIP bias values in the active region, with the interquartile range of the distribution extending from 1.34–3.73, with a tail of values reaching ~ 10 . The median FIP bias value here is at 2.21, much lower than that expected for active regions, which is surprising given that the Ca XIV/Ar XIV diagnostic is much more sensitive to the hotter plasma expected in active regions of the solar atmosphere. The distribution of the bulk of the FIP bias values for the Fe XVI/S XIII diagnostic is much narrower, with the interquartile range extending from 1.73–2.73, but with a median value of 2.12 comparable to that of the corresponding Quiet Sun region.

(b) Examining the signal-to-noise ratio

Although the images shown in the top row of Figure 2 suggest that the three FIP bias ratios measured provide distinct measurements for the different regions across the solar disk, the Fe XVI/S XIII and Ca XIV/Ar XIV ratios are high-temperature emission lines that should produce little to no measurable signal in quiet Sun regions and coronal holes in particular [cf. 41]. To investigate this further, we examined the different FIP bias ratios using a filtering method to

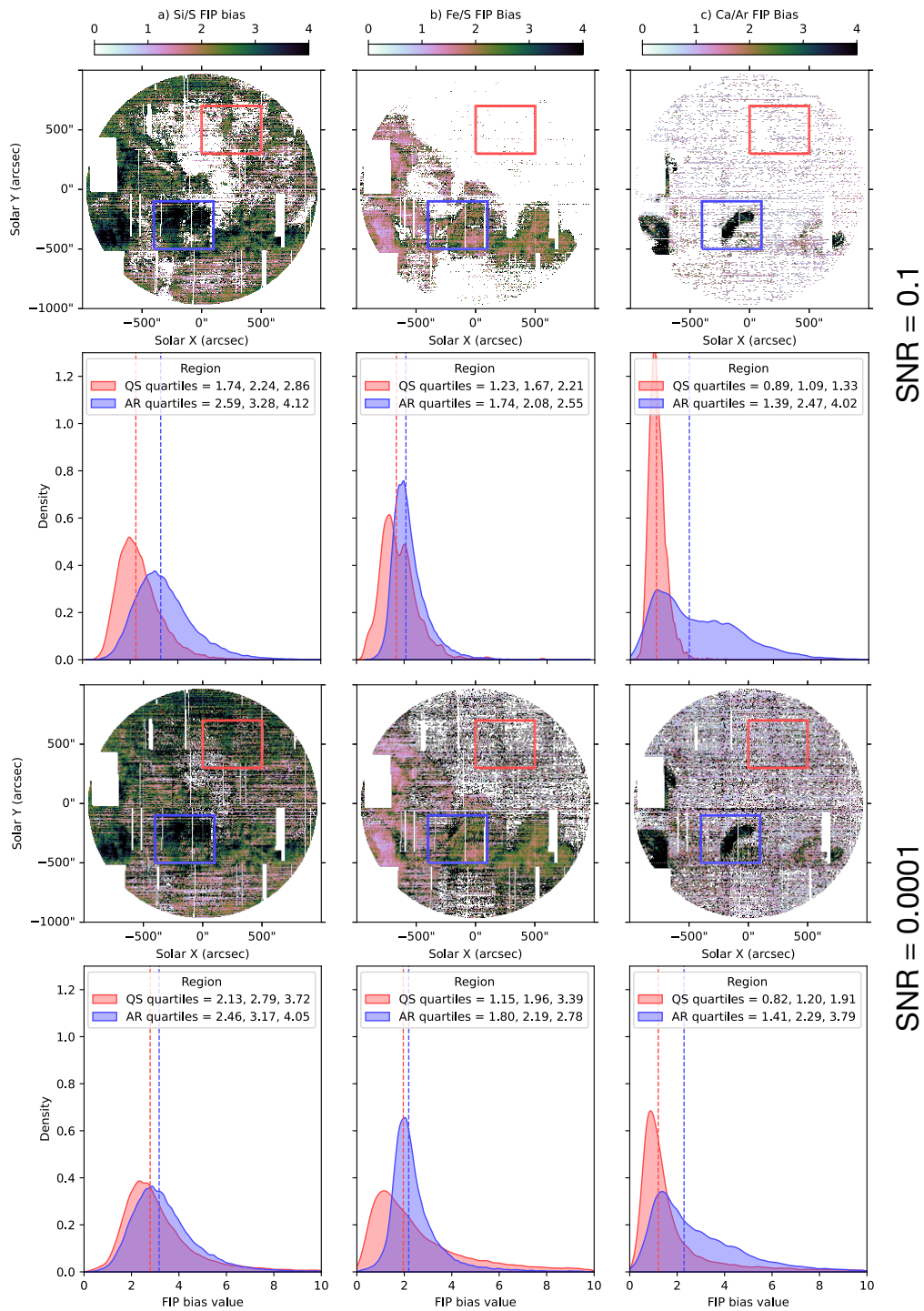


Figure 3. *Hinode*/EIS full disk mosaics and corresponding KDE plots for signal-to-noise cutoffs of 0.1 (upper two rows) and 0.0001 (bottom two rows). In each case, the FIP bias ratios are (from left to right) Si X/S X, Fe XVI/S XIII, and Ca XIV/Ar XIV.

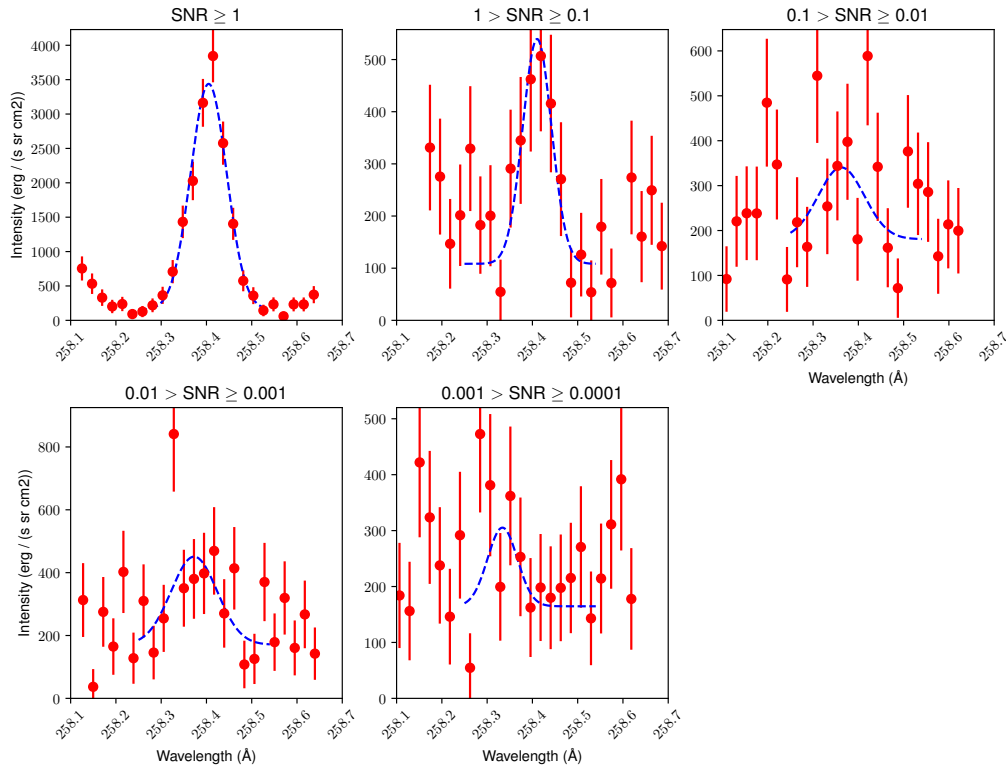


Figure 4. A comparison of fits to the Si X 258.37 Å spectral line for different ranges of the signal-to-noise (in each case given in the panel title).

remove pixels with a signal-to-noise ratio below a range of pre-defined levels. This approach ensures that only pixels with a sufficiently strong signal in the different lines used to estimate the FIP bias ratios were considered in each case. It also enables a better understanding of the distribution of FIP bias values in the regions of interest examined in this work.

The signal-to-noise ratio (SNR) for each pixel was estimated by first subtracting the fit to the intensity for the individual spectral lines from the observed intensity to calculate the residuals. The SNR was then taken as the spectral intensity divided by the standard deviation of the residuals σ_{res} as so;

$$SNR = \frac{I - fit}{\sigma_{res}}. \quad (3.1)$$

We then defined a range of cutoff values, in each case only including those pixels with an SNR above the cutoff for each wavelength. Figure 3 shows the corresponding images and KDE plots of the regions of interest for the different FIP bias ratios studied assuming a SNR cutoff of 0.1 (upper two rows) and 0.0001 (bottom two rows).

To fully examine the importance of filtering FIP bias estimates by comparing signal-to-noise values, a range of SNR cutoff values from high to very low values that approximated noise were examined as part of this work. A SNR cutoff of 5 meant that no valid data was returned for any wavelength considered here, whereas a SNR cutoff of 1 only revealed a small number of useable pixels scattered throughout the Si X/S X and Fe XVI/S XIII FIP bias images. Using a SNR cutoff of 0.1 (as shown in Figure 3) provides a much larger number of useable pixels, particularly in the Si X/S X image and distribution. The white area seen in the top left panel of Figure 3 corresponds to a coronal hole, with a correspondingly low observable signal. For the Fe XVI/S XIII and particularly the Ca XIV/Ar XIV FIP bias ratios, there is very little signal outside the active regions,

with very narrow associated distributions of values for the quiet Sun regions in the corresponding KDE plots. It is interesting that the KDE for the Ca XIV/Ar XIV active region appears to have two peaks, with the image showing a very strong signal in the core of the active region and a weaker signal in the outer part of the active region. Figure 4 shows the fit to the Si X 258.37 Å spectral line for different ranges of the signal-to-noise ratio studied here. As expected, the fit to the spectral line for SNR>1 is quite good, with the fits to the spectral line becoming progressively worse for lower SNR ranges.

Decreasing the SNR cutoff to 0.0001 (bottom two rows of Figure 3) produces a set of FIP bias images much closer to that seen in Figure 2, for which no SNR filtering has been applied. The Si X/S X image has not changed much, albeit with the inclusion of more signal in the coronal hole region. The associated KDE plots show that the distributions of values from the Quiet Sun and active region are much closer together with the lower SNR cutoff, although the median values of the distributions are still comparable. For the Fe XVI/S XIII FIP bias, there are now many more useable pixels across the quiet Sun, with a much smoother distribution of values in the KDE plots for both Quiet Sun and active region. However, the median values of both distributions remain comparable. Finally, the Ca XIV/Ar XIV image again shows many more useable pixels across the solar disk, with the previously twin peaked active region KDE plot now smoothed out to produce a more gradually decreasing slope towards higher FIP values. Again, the median FIP bias values are comparable in each case.

It is interesting that the KDE distributions for the lower SNR cutoff have much longer tails of higher FIP bias values, indicating that more noisy pixels producing spurious FIP bias values are now being counted and included in the distributions. However, the choice of median rather than mean to estimate a single value for the FIP bias negates this trend, giving estimated single FIP bias values that are effectively unchanged for different SNR cutoff values.

4. Discussion & Conclusions

As mass and energy evolve through the solar atmosphere into the heliosphere, the properties of the plasma change and evolve as the result of turbulence, heating, mass motion, and elemental fractionation. While temperature, density, and other plasma properties can change as the plasma propagates out into the heliosphere, the FIP bias of the plasma remains fixed, imprinted by the properties of the region where the plasma was initially fractionated. This makes FIP bias a valuable diagnostic tool for tracking and quantifying the evolution of plasma from the Sun into the heliosphere, enabling a connection to be made between remote-sensing observations of the Sun and direct measurements of the solar wind *in-situ* at spacecraft throughout the heliosphere. The *Solar Orbiter* spacecraft in particular has been designed to leverage this plasma property and thus maximise the scientific return, while it also has important implications for the forecasting and understanding of space weather and the effect of the Sun on the near-Earth environment.

FIP bias measurements of different parts of the solar atmosphere are typically given as single values, with active regions, quiet Sun, and coronal holes typically quoted as having FIP bias values of ~ 3 , ~ 1.5 -2 and ~ 1 respectively [14]. This can be interpreted as active regions having coronal composition, coronal holes having photospheric composition, and the quiet Sun having a composition that lies between coronal and photospheric values. However FIP bias does not have a single unique measurement, as any combination of low and high FIP elements can be used to estimate FIP bias [accounting for comparable emissivities, temperature, and density effects, e.g., 25]. As a result, there are multiple potential line pairs within the spectral window observed by the *Hinode*/EIS instrument that can and have been used to observe the solar corona. Although the Si X/S X diagnostic is the most commonly used, it is also possible to use the Ca XIV/Ar XIV and Fe XVI/S XIII line pairs to estimate the FIP bias, with each line pair sensitive to plasma at slightly different temperatures.

Previous work [17] has suggested that FIP bias may be best observed as a distribution rather than the commonly used single value approach. This has implications for how it can be used to relate plasma observed on the Sun with plasma detected *in-situ* (e.g., as by the *Solar Orbiter*

spacecraft), and as a result requires further investigation. In this work we used full disk mosaic spectral scans of the Sun to compare FIP bias measurements using three different diagnostics; Si X/S X, Ca XIV/Ar XIV, and Fe XVI/S XIII. As shown in Figure 2, the full disk spectral scans highlight the different regions of the solar disk, because each spectral line has different temperature sensitivities, allowing the active region and quiet sun to be distinguished. While each diagnostic was applied to the full disk, as shown in Figure 2 the Si X/S X diagnostic, sensitive to coronal plasma of $\sim 1\text{--}2$ MK, has signal and measurable FIP bias in both the Quiet Sun and active regions, whereas the Ca XIV/Ar XIV diagnostic, sensitive to hot plasma of $\sim 3\text{--}4$ MK exhibits a clear FIP bias primarily in the active regions. The Fe XVI/S XIII diagnostic is sensitive to plasma between these two extremes, identifying the full extent of the active regions rather than just the cores seen using the Ca XIV/Ar XIV diagnostic.

However, a different picture emerges when considering the distribution of values within regions of interest defined to compare the quiet Sun and active regions. As shown in Figure 2, the distributions of FIP bias values measured in the quiet Sun tends to peak at a slightly lower value than the distribution in the active region. It is notable that the bulk of the FIP bias values in the active region distributions are lower than three for the Ca XIV/Ar XIV and Fe XVI/S XIII diagnostics. The choice of elements and lines used to estimate the FIP bias is also interesting and worth considering when trying to compare the different regions of interest. The three diagnostics examined here were chosen as they are well observed by *Hinode*/EIS and are therefore commonly used to produce spatially resolved FIP bias maps of the solar atmosphere. However, the results described here show that there are distinct variations between the individual diagnostics which must be acknowledged when comparing them, with each diagnostic affected differently by variations in plasma properties such as temperature and density. In addition, the three diagnostics are derived in slightly different ways, with a DEM technique used to derive the Si X/S X and Fe XVI/S XIII diagnostics while the Ca XIV/Ar XIV diagnostic is typically derived using an intensity ratio approach due to the comparable contribution functions of the two spectral lines. This could also contribute to the observed differences, although [32] previously found that the intensity ratio approach was comparable to the DEM approach for the Ca XIV/Ar XIV diagnostic. Work elsewhere in this special issue has also highlighted important characteristics of the plasma to consider when comparing different diagnostics. In particular, [42] suggest that the behaviour of Sulphur is sensitive to the ambient magnetic field strength, while work by [43] also in this special issue shows the importance of considering the temporal evolution of ionisation fraction when working with elemental abundances.

In addition, the visual representation of the derived FIP bias can be affected by the assumed signal-to-noise ratio used to discount noisy pixels or pixels with no useable signals. The DEM technique commonly used to derive the Si X/S X and Fe XVI/S XIII diagnostics discounts pixels where the Markov Chain Monte Carlo analysis has a χ^2 value greater than the number of lines used for the calculation [cf. 14, 44]. However, filtering of data assuming a defined signal-to-noise ratio is not typically performed. Figure 3 compares the different FIP bias ratios for varying SNR values of 0.1 and 0.0001, finding that while the different SNR cutoff values clearly affect the the FIP bias maps and the number of useable pixels in each case, the corresponding KDE distributions are largely unaffected. A lower SNR cutoff contributes more noisy pixels with higher FIP bias values to the KDE distributions, producing a longer tail on the distributions. However, despite the inclusion of more high FIP bias values, the median values of the distributions exhibits very little change. A comparison of the fits to the Si X 258.37 Å spectral line for different ranges of the signal-to-noise is shown in Figure 4. It is clear that the quality of fits to the spectral lines decreases with lower SNR ranges, underlining the importance of checking individual fits and ensuring a robust approach to including pixels with lower SNR when undertaking this analysis. Note that the SNR cutoff values yielding “useable” measurements here are much lower than those used in other contexts. The aim here is to highlight the importance of understanding the data and its limitations, and ensuring the correct use of appropriate diagnostics when comparing different regions of the solar atmosphere. It is also worth noting that previous work by [41] found negligible emission

from quiet Sun and coronal holes in higher temperature spectral lines observed by EIS. Instead, they suggested that corresponding signal in these lines must be scattered light from nearby active regions.

These results indicate the importance of examining fully all aspects of the data when using FIP bias ratios. It is misleading to quote a fixed FIP bias value rather than a distribution when considering plasma fractionation and to quote fixed FIP bias values for defined regions of the solar atmosphere based on a single line pair diagnostic. Instead, this work shows that quoting the quartiles of the FIP bias distribution for a given region of interest may be more useful, as this makes no assumptions of the shape of the distribution, provides an indication of its width and asymmetry, and enables a more statistically rigorous analysis of the distributions. Previous work by [14] did derive an uncertainty of ~ 0.3 for FIP bias measurements given the uncertainty in EIS intensity measurements and the nature of the MCMC DEM approach that they used. However, the distributions of FIP bias values presented here show significantly more variation, suggesting that while the uncertainty derived by [14] may be correct for an individual pixel, the quartile approach may provide a more holistic estimate of the uncertainty within a region of interest. The signal-to-noise of the data must also be considered, as the work discussed here shows that it offers an additional check on the validity of the FIP bias diagnostic, particularly in regions with a temperature outside the optimal temperature range of the diagnostic being used.

As our understanding of the processes by which plasma is fractionated and transported through the solar atmosphere improve and evolve, it will be possible to better characterise the FIP bias of the different regions of the solar corona. The improved spectral, spatial, and temporal resolution of next generation instrumentation such as Solar-C EUVST and the ongoing work linking the Sun to the heliosphere with *Solar Orbiter* [3] will help in that regard.

Data Accessibility. No new data were generated as part of this study. The Hinode EIS data can be downloaded from the Hinode Science Data Centre (<http://sdc.uio.no/sdc/>)

Authors' Contributions. DML conceived the study. KDS carried out the data reduction and scientific analysis with assistance from DML. ASHT processed the Fe XVI/S XIII data. DML drafted the manuscript with help from KDS. All authors read and approved the manuscript.

Competing Interests. The author(s) declare that they have no competing interests.

Funding.

Acknowledgements. The authors wish to thank the referee whose suggestions helped to improve the paper. We thank the Royal Society for its support throughout the organization of the Theo Murphy meeting on "Solar Abundances in Space and Time" and production of this special issue. ASHT acknowledge support through the European Space Agency (ESA) Research Fellowship Programme in Space Science. Hinode is a Japanese mission developed and launched by ISAS/JAXA, collaborating with NAOJ as a domestic partner, and NASA and STFC (UK) as international partners. Scientific operation of Hinode is performed by the Hinode science team organized at ISAS/JAXA. Support for the post-launch operation is provided by JAXA and NAOJ (Japan), STFC (UK), NASA, ESA, and NSC (Norway). This research used the following software packages during analysis of the data and preparation of this paper: Numpy [45], Scipy [46], SunPy [47], Seaborn [48], Matplotlib [49], Astropy [50], eispac [24].

References

1. Asplund M, Grevesse N, Sauval AJ, Scott P. 2009 The Chemical Composition of the Sun. *Annu. Rev. Astron. Astrophys.* **47**, 481–522. ([10.1146/annurev.astro.46.060407.145222](https://doi.org/10.1146/annurev.astro.46.060407.145222))
2. Meyer JP. 1985 The baseline composition of solar energetic particles. *Astrophys. J. Suppl. Ser.* **57**, 151–171. ([10.1086/191000](https://doi.org/10.1086/191000))
3. Yardley SL, Brooks DH, D'Amicis R, Owen CJ, Long DM, Baker D, Démoulin P, Owens MJ, Lockwood M, Mihalescu T, Coburn JT, Dewey RM, Müller D, Suen GHH, Ngampoopun N, Louarn P, Livi S, Lepri S, Fludra A, Haberreiter M, Schühle U. 2024 Multi-source connectivity

- as the driver of solar wind variability in the heliosphere. *Nature Astronomy* **8**, 953–963. ([10.1038/s41550-024-02278-9](https://doi.org/10.1038/s41550-024-02278-9))
4. Müller D, St. Cyr OC, Zouganelis I, Gilbert HR, Marsden R, Nieves-Chinchilla T, Antonucci E, Auchère F, Berghmans D, Horbury TS, Howard RA, Krucker S, Maksimovic M, Owen CJ, Rochus P, Rodriguez-Pacheco J, Romoli M, Solanki SK, Bruno R, Carlsson M, Fludra A, Harra L, Hassler DM, Livi S, Louarn P, Peter H, Schühle U, Teriaca L, del Toro Iniesta JC, Wimmer-Schweingruber RF, Marsch E, Velli M, De Groof A, Walsh A, Williams D. 2020 The Solar Orbiter mission. Science overview. *Astron. Astrophys.* **642**, A1. ([10.1051/0004-6361/202038467](https://doi.org/10.1051/0004-6361/202038467))
 5. Laming JM. 2015 The FIP and Inverse FIP Effects in Solar and Stellar Coronae. *Living Reviews in Solar Physics* **12**, 2. ([10.1007/lrsp-2015-2](https://doi.org/10.1007/lrsp-2015-2))
 6. Stangalini M, Baker D, Valori G, Jess DB, Jafarzadeh S, Murabito M, To ASH, Brooks DH, Ermolli I, Giorgi F, MacBride CD. 2021 Spectropolarimetric fluctuations in a sunspot chromosphere. *Philosophical Transactions of the Royal Society of London Series A* **379**, 20200216. ([10.1098/rsta.2020.0216](https://doi.org/10.1098/rsta.2020.0216))
 7. Murabito M, Stangalini M, Laming JM, Baker D, To ASH, Long DM, Brooks DH, Jafarzadeh S, Jess DB, Valori G. 2024 Observation of Alfvén Wave Reflection in the Solar Chromosphere: Ponderomotive Force and First Ionization Potential Effect. *Phys. Rev. Lett.* **132**, 215201. ([10.1103/PhysRevLett.132.215201](https://doi.org/10.1103/PhysRevLett.132.215201))
 8. Baker D, Stangalini M, Valori G, Brooks DH, To ASH, van Driel-Gesztelyi L, Démoulin P, Stansby D, Jess DB, Jafarzadeh S. 2021 Alfvénic Perturbations in a Sunspot Chromosphere Linked to Fractionated Plasma in the Corona. *Astrophys. J.* **907**, 16. ([10.3847/1538-4357/abcafd](https://doi.org/10.3847/1538-4357/abcafd))
 9. Murabito M, Stangalini M, Baker D, Valori G, Jess DB, Jafarzadeh S, Brooks DH, Ermolli I, Giorgi F, Grant SDT, Long DM, van Driel-Gesztelyi L. 2021 Investigating the origin of magnetic perturbations associated with the FIP Effect. *Astron. Astrophys.* **656**, A87. ([10.1051/0004-6361/202141504](https://doi.org/10.1051/0004-6361/202141504))
 10. Long DM, Baker D, To ASH, van Driel-Gesztelyi L, Brooks DH, Stangalini M, Murabito M, James AW, Mathioudakis M, Testa P. 2024 Identifying Plasma Fractionation Processes in the Chromosphere Using IRIS. *Astrophys. J.* **965**, 63. ([10.3847/1538-4357/ad3234](https://doi.org/10.3847/1538-4357/ad3234))
 11. Testa P, Martínez-Sykora J, De Pontieu B. 2023 Coronal Abundances in an Active Region: Evolution and Underlying Chromospheric and Transition Region Properties. *Astrophys. J.* **944**, 117. ([10.3847/1538-4357/acb343](https://doi.org/10.3847/1538-4357/acb343))
 12. Culhane JL, Harra LK, James AM, Al-Janabi K, Bradley LJ, Chaudry RA, Rees K, Tandy JA, Thomas P, Whillock MCR, Winter B, Doschek GA, Korendyke CM, Brown CM, Myers S, Mariska J, Seely J, Lang J, Kent BJ, Shaughnessy BM, Young PR, Simnett GM, Castelli CM, Mahmoud S, Mapson-Menard H, Probyn BJ, Thomas RJ, Davila J, Dere K, Windt D, Shea J, Hagood R, Moye R, Hara H, Watanabe T, Matsuzaki K, Kosugi T, Hansteen V, Wikstol Ø. 2007 The EUV Imaging Spectrometer for Hinode. *Sol. Phys.* **243**, 19–61. ([10.1007/s01007-007-0293-1](https://doi.org/10.1007/s01007-007-0293-1))
 13. Kosugi T, Matsuzaki K, Sakao T, Shimizu T, Sone Y, Tachikawa S, Hashimoto T, Minesugi K, Ohnishi A, Yamada T, Tsuneta S, Hara H, Ichimoto K, Suematsu Y, Shimojo M, Watanabe T, Shimada S, Davis JM, Hill LD, Owens JK, Title AM, Culhane JL, Harra LK, Doschek GA, Golub L. 2007 The Hinode (Solar-B) Mission: An Overview. *Sol. Phys.* **243**, 3–17. ([10.1007/s11207-007-9014-6](https://doi.org/10.1007/s11207-007-9014-6))
 14. Brooks DH, Ugarte-Urra I, Warren HP. 2015 Full-Sun observations for identifying the source of the slow solar wind. *Nature Communications* **6**, 5947. ([10.1038/ncomms6947](https://doi.org/10.1038/ncomms6947))
 15. Baker D, Brooks DH, van Driel-Gesztelyi L, James AW, Démoulin P, Long DM, Warren HP, Williams DR. 2018 Coronal Elemental Abundances in Solar Emerging Flux Regions. *Astrophys. J.* **856**, 71. ([10.3847/1538-4357/aaadb0](https://doi.org/10.3847/1538-4357/aaadb0))
 16. Baker D, Brooks DH, Démoulin P, van Driel-Gesztelyi L, Green LM, Steed K, Carlyle J. 2013 Plasma Composition in a Sigmoidal Anemone Active Region. *Astrophys. J.* **778**, 69. ([10.1088/0004-637X/778/1/69](https://doi.org/10.1088/0004-637X/778/1/69))
 17. Mihailescu T, Baker D, Green LM, van Driel-Gesztelyi L, Long DM, Brooks DH, To ASH. 2022 What Determines Active Region Coronal Plasma Composition?. *Astrophys. J.* **933**, 245. ([10.3847/1538-4357/ac6e40](https://doi.org/10.3847/1538-4357/ac6e40))
 18. To ASH, James AW, Bastian TS, van Driel-Gesztelyi L, Long DM, Baker D, Brooks DH,

- Lomuscio S, Stansby D, Valori G. 2023 Understanding the Relationship between Solar Coronal Abundances and F10.7 cm Radio Emission. *Astrophys. J.* **948**, 121. ([10.3847/1538-4357/acbc1b](https://doi.org/10.3847/1538-4357/acbc1b))
19. Feldman U, Widing KG. 1993 Elemental Abundances in the Upper Solar Atmosphere of Quiet and Coronal Hole Regions (T E 4.3 X 10 5 K). *Astrophys. J.* **414**, 381. ([10.1086/173084](https://doi.org/10.1086/173084))
 20. SPICE Consortium, Anderson M, Appourchaux T, Auchère F, Aznar Cuadrado R, Barbay J, Baudin F, Beardsley S, Bocchialini K, Borgo B, Bruzzi D, Buchlin E, Burton G, Büchel V, Caldwell M, Caminade S, Carlsson M, Curdt W, Davenne J, Davila J, Deforest CE, Del Zanna G, Drummond D, Dubau J, Dumesnil C, Dunn G, Eccleston P, Fludra A, Fredvik T, Gabriel A, Giunta A, Gottwald A, Griffin D, Grundy T, Guest S, Gyo M, Haberreiter M, Hansteen V, Harrison R, Hassler DM, Haugan SVH, Howe C, Janvier M, Klein R, Koller S, Kucera TA, Kouliche D, Marsch E, Marshall A, Marshall G, Matthews SA, McQuirk C, Meining S, Mercier C, Morris N, Morse T, Munro G, Parenti S, Pastor-Santos C, Peter H, Pfiffner D, Phelan P, Philippon A, Richards A, Rogers K, Sawyer C, Schlatter P, Schmutz W, Schühle U, Shaughnessy B, Sidher S, Solanki SK, Speight R, Spescha M, Szwec N, Tamiatto C, Teriaca L, Thompson W, Tosh I, Tustain S, Vial JC, Walls B, Waltham N, Wimmer-Schweingruber R, Woodward S, Young P, de Groof A, Pacros A, Williams D, Müller D. 2020 The Solar Orbiter SPICE instrument. An extreme UV imaging spectrometer. *Astron. Astrophys.* **642**, A14. ([10.1051/0004-6361/201935574](https://doi.org/10.1051/0004-6361/201935574))
 21. Owen CJ, Bruno R, Livi S, Louarn P, Al Janabi K, Allegrini F, Amoros C, Baruah R, Barthe A, Berthomier M, Bordon S, Brockley-Blatt C, Brysbaert C, Capuano G, Collier M, DeMarco R, Fedorov A, Ford J, Fortunato V, Fratter I, Galvin AB, Hancock B, Heirtzler D, Kataria D, Kistler L, Lepri ST, Lewis G, Loeffler C, Marty W, Mathon R, Mayall A, Mele G, Ogasawara K, Orlandi M, Pacros A, Penou E, Persyn S, Petiot M, Phillips M, Přeč L, Raines JM, Reden M, Rouillard AP, Rousseau A, Rubiella J, Seran H, Spencer A, Thomas JW, Trevino J, Verscharen D, Wurz P, Alapide A, Amoroso L, André N, Anekallu C, Arciuli V, Arnett KL, Ascolese R, Bancroft C, Bland P, Brysch M, Calvanese R, Castronuovo M, Čermák I, Chornay D, Clemens S, Coker J, Collinson G, D'Amicis R, Dandouras I, Darnley R, Davies D, Davison G, De Los Santos A, Devoto P, Dirks G, Edlund E, Fazakerley A, Ferris M, Frost C, Fruit G, Garat C, Génot V, Gibson W, Gilbert JA, de Giosa V, Gradone S, Hailey M, Horbury TS, Hunt T, Jacquy C, Johnson M, Lavraud B, Lawrenson A, Leblanc F, Lockhart W, Maksimovic M, Malpus A, Marcucci F, Mazelle C, Monti F, Myers S, Nguyen T, Rodriguez-Pacheco J, Phillips I, Popecki M, Rees K, Rogacki SA, Ruane K, Rust D, Salatti M, Sauvaud JA, Stakhiv MO, Stange J, Stubbs T, Taylor T, Techer JD, Terrier G, Thibodeaux R, Urdiales C, Varsani A, Walsh AP, Watson G, Wheeler P, Willis G, Wimmer-Schweingruber RF, Winter B, Yardley J, Zouganelis I. 2020 The Solar Orbiter Solar Wind Analyser (SWA) suite. *Astron. Astrophys.* **642**, A16. ([10.1051/0004-6361/201937259](https://doi.org/10.1051/0004-6361/201937259))
 22. Del Zanna G, Mason HE. 2014 Elemental abundances and temperatures of quiescent solar active region cores from X-ray observations. *Astron. Astrophys.* **565**, A14. ([10.1051/0004-6361/201423471](https://doi.org/10.1051/0004-6361/201423471))
 23. Ko YK, Young PR, Muglach K, Warren HP, Ugarte-Urra I. 2016 Correlation of Coronal Plasma Properties and Solar Magnetic Field in a Decaying Active Region. *Astrophys. J.* **826**, 126. ([10.3847/0004-637X/826/2/126](https://doi.org/10.3847/0004-637X/826/2/126))
 24. Weberg M, Warren H, Crump N, Barnes W. 2023 EISPAC - The EIS Python Analysis Code. *The Journal of Open Source Software* **8**, 4914. ([10.21105/joss.04914](https://doi.org/10.21105/joss.04914))
 25. Feldman U, Warren HP, Brown CM, Doschek GA. 2009 Can the Composition of the Solar Corona Be Derived from Hinode/Extreme-Ultraviolet Imaging Spectrometer Spectra?. *Astrophys. J.* **695**, 36–45. ([10.1088/0004-637X/695/1/36](https://doi.org/10.1088/0004-637X/695/1/36))
 26. To ASH, Long DM, Baker D, Brooks DH, van Driel-Gesztelyi L, Laming JM, Valori G. 2021 The Evolution of Plasma Composition during a Solar Flare. *Astrophys. J.* **911**, 86. ([10.3847/1538-4357/abe85a](https://doi.org/10.3847/1538-4357/abe85a))
 27. Dere KP, Landi E, Mason HE, Monsignori Fossi BC, Young PR. 1997 CHIANTI - an atomic database for emission lines. *Astron. Astrophys. Suppl. Ser.* **125**, 149–173. ([10.1051/aas:1997368](https://doi.org/10.1051/aas:1997368))
 28. Del Zanna G, Dere KP, Young PR, Landi E. 2021 CHIANTI—An Atomic Database for Emission Lines. XVI. Version 10, Further Extensions. *Astrophys. J.* **909**, 38. ([10.3847/1538-4357/abd8ce](https://doi.org/10.3847/1538-4357/abd8ce))

29. Scott P, Grevesse N, Asplund M, Sauval AJ, Lind K, Takeda Y, Collet R, Trampedach R, Hayek W. 2015a The elemental composition of the Sun. I. The intermediate mass elements Na to Ca. *Astron. Astrophys.* **573**, A25. ([10.1051/0004-6361/201424109](https://doi.org/10.1051/0004-6361/201424109))
30. Scott P, Asplund M, Grevesse N, Bergemann M, Sauval AJ. 2015b The elemental composition of the Sun. II. The iron group elements Sc to Ni. *Astron. Astrophys.* **573**, A26. ([10.1051/0004-6361/201424110](https://doi.org/10.1051/0004-6361/201424110))
31. Warren HP, Ugarte-Urra I, Landi E. 2014 The Absolute Calibration of the EUV Imaging Spectrometer on Hinode. *Astrophys. J. Suppl. Ser.* **213**, 11. ([10.1088/0067-0049/213/1/11](https://doi.org/10.1088/0067-0049/213/1/11))
32. Baker D, van Driel-Gesztelyi L, Brooks DH, Valori G, James AW, Laming JM, Long DM, Démoulin P, Green LM, Matthews SA, Oláh K, Kóvári Z. 2019 Transient Inverse-FIP Plasma Composition Evolution within a Solar Flare. *Astrophys. J.* **875**, 35. ([10.3847/1538-4357/ab07c1](https://doi.org/10.3847/1538-4357/ab07c1))
33. Doschek GA, Warren HP, Feldman U. 2015 Anomalous Relative Ar/Ca Coronal Abundances Observed by the Hinode/EUV Imaging Spectrometer Near Sunspots. *Astrophys. J. Lett.* **808**, L7. ([10.1088/2041-8205/808/1/L7](https://doi.org/10.1088/2041-8205/808/1/L7))
34. Doschek GA, Warren HP. 2016 The Mysterious Case of the Solar Argon Abundance near Sunspots in Flares. *Astrophys. J.* **825**, 36. ([10.3847/0004-637X/825/1/36](https://doi.org/10.3847/0004-637X/825/1/36))
35. Doschek GA, Warren HP. 2017 Sunspots, Starspots, and Elemental Abundances. *Astrophys. J.* **844**, 52. ([10.3847/1538-4357/aa7bea](https://doi.org/10.3847/1538-4357/aa7bea))
36. Baker D, Green LM, Brooks DH, Démoulin P, van Driel-Gesztelyi L, Mihailescu T, To ASH, Long DM, Yardley SL, Janvier M, Valori G. 2022 Evolution of Plasma Composition in an Eruptive Flux Rope. *Astrophys. J.* **924**, 17. ([10.3847/1538-4357/ac32d2](https://doi.org/10.3847/1538-4357/ac32d2))
37. To ASH, Brooks DH, Imada S, French RJ, van Driel-Gesztelyi L, Baker D, Long DM, Ashfield, IV W, Hayes LA. 2024 Spatially resolved plasma composition evolution in a solar flare – The effect of reconnection outflow. *Astron. Astrophys.* **691**, A95. ([10.1051/0004-6361/202449246](https://doi.org/10.1051/0004-6361/202449246))
38. Silverman BW. 1986 *Density estimation for statistics and data analysis*.
39. Dacie S, Démoulin P, van Driel-Gesztelyi L, Long DM, Baker D, Janvier M, Yardley SL, Pérez-Suárez D. 2016 Evolution of the magnetic field distribution of active regions. *Astron. Astrophys.* **596**, A69. ([10.1051/0004-6361/201628948](https://doi.org/10.1051/0004-6361/201628948))
40. de Jager OC, Raubenheimer BC, Swanepoel JWH. 1986 Kernel density estimations applied to gamma ray light curves. *Astron. Astrophys.* **170**, 187–196.
41. Young PR, Viall NM. 2022 Scattered Light in the Hinode/EIS and SDO/AIA Instruments Measured from the 2012 Venus Transit. *Astrophys. J.* **938**, 27. ([10.3847/1538-4357/ac8472](https://doi.org/10.3847/1538-4357/ac8472))
42. Orlovskij D, To ASH, Long DM. 2025 Signs of Sulphur fractionation under high magnetic field strength. *Phil. Trans. Royal Soc. A*.
43. Reep JW, Benavitz LF, To ASH, Brooks DH, Laming JM, Antolin P, Long DM, Baker D, Tarr LA. 2025 Radiative hydrodynamic simulations of FIP fractionation in solar flares. *Phil. Trans. Royal Soc. A*.
44. Brooks DH, Warren HP. 2011 Establishing a Connection Between Active Region Outflows and the Solar Wind: Abundance Measurements with EIS/Hinode. *Astrophys. J. Lett.* **727**, L13. ([10.1088/2041-8205/727/1/L13](https://doi.org/10.1088/2041-8205/727/1/L13))
45. Harris CR, Millman KJ, van der Walt SJ, Gommers R, Virtanen P, Cournapeau D, Wieser E, Taylor J, Berg S, Smith NJ, Kern R, Picus M, Hoyer S, van Kerkwijk MH, Brett M, Haldane A, del Río JF, Wiebe M, Peterson P, Gérard-Marchant P, Sheppard K, Reddy T, Weckesser W, Abbasi H, Gohlke C, Oliphant TE. 2020 Array programming with NumPy. *Nature* **585**, 357–362. ([10.1038/s41586-020-2649-2](https://doi.org/10.1038/s41586-020-2649-2))
46. Virtanen P, Gommers R, Oliphant TE, Haberland M, Reddy T, Cournapeau D, Burovski E, Peterson P, Weckesser W, Bright J, van der Walt SJ, Brett M, Wilson J, Millman KJ, Mayorov N, Nelson ARJ, Jones E, Kern R, Larson E, Carey CJ, Polat İ, Feng Y, Moore EW, VanderPlas J, Laxalde D, Perktold J, Cimrman R, Henriksen I, Quintero EA, Harris CR, Archibald AM, Ribeiro AH, Pedregosa F, van Mulbregt P, SciPy 1.0 Contributors. 2020 SciPy 1.0: Fundamental Algorithms for Scientific Computing in Python. *Nature Methods* **17**, 261–272. ([10.1038/s41592-019-0686-2](https://doi.org/10.1038/s41592-019-0686-2))
47. The SunPy Community, Barnes WT, Bobra MG, Christe SD, Freij N, Hayes LA, Ireland J, Mumford S, Perez-Suarez D, Ryan DF, Shih AY, Chanda P, Glogowski K, Hewett R, Hughitt

- VK, Hill A, Hiware K, Inglis A, Kirk MSF, Konge S, Mason JP, Maloney SA, Murray SA, Panda A, Park J, Pereira TMD, Reardon K, Savage S, Sipőcz BM, Stansby D, Jain Y, Taylor G, Yadav T, Rajul, Dang TK. 2020 The SunPy Project: Open Source Development and Status of the Version 1.0 Core Package. *The Astrophysical Journal* **890**, 68–. ([10.3847/1538-4357/ab4f7a](https://doi.org/10.3847/1538-4357/ab4f7a))
48. Waskom ML. 2021 seaborn: statistical data visualization. *Journal of Open Source Software* **6**, 3021. ([10.21105/joss.03021](https://doi.org/10.21105/joss.03021))
49. Hunter JD. 2007 Matplotlib: A 2D graphics environment. *Computing in Science & Engineering* **9**, 90–95. ([10.1109/MCSE.2007.55](https://doi.org/10.1109/MCSE.2007.55))
50. Astropy Collaboration, Price-Whelan AM, Lim PL, Earl N, Starkman N, Bradley L, Shupe DL, Patil AA, Corrales L, Brasseur CE, Nöthe M, Donath A, Tollerud E, Morris BM, Ginsburg A, Vaher E, Weaver BA, Tocknell J, Jamieson W, van Kerkwijk MH, Robitaille TP, Merry B, Bachetti M, Günther HM, Aldcroft TL, Alvarado-Montes JA, Archibald AM, Bódi A, Bapat S, Barentsen G, Bazán J, Biswas M, Boquien M, Burke DJ, Cara D, Cara M, Conroy KE, Conseil S, Craig MW, Cross RM, Cruz KL, D'Eugenio F, Dencheva N, Devillepoix HAR, Dietrich JP, Eigenbrot AD, Erben T, Ferreira L, Foreman-Mackey D, Fox R, Freij N, Garg S, Geda R, Glattly L, Gondhalekar Y, Gordon KD, Grant D, Greenfield P, Groener AM, Guest S, Gurovich S, Handberg R, Hart A, Hatfield-Dodds Z, Homeier D, Hosseinzadeh G, Jenness T, Jones CK, Joseph P, Kalmbach JB, Karamehmetoglu E, Kałuszyński M, Kelley MSP, Kern N, Kerzendorf WE, Koch EW, Kulumani S, Lee A, Ly C, Ma Z, MacBride C, Maljaars JM, Muna D, Murphy NA, Norman H, O'Steen R, Oman KA, Pacifici C, Pascual S, Pascual-Granado J, Patil RR, Perren GI, Pickering TE, Rastogi T, Roulston BR, Ryan DF, Rykoff ES, Sabater J, Sakurikar P, Salgado J, Sanghi A, Saunders N, Savchenko V, Schwardt L, Seifert-Eckert M, Shih AY, Jain AS, Shukla G, Sick J, Simpson C, Singanamalla S, Singer LP, Singhal J, Sinha M, Sipőcz BM, Spitler LR, Stansby D, Streicher O, Šumak J, Swinbank JD, Taranu DS, Tewary N, Tremblay GR, de Val-Borro M, Van Kooten SJ, Vasović Z, Verma S, de Miranda Cardoso JV, Williams PKG, Wilson TJ, Winkel B, Wood-Vasey WM, Xue R, Yoachim P, Zhang C, Zonca A, Astropy Project Contributors. 2022 The Astropy Project: Sustaining and Growing a Community-oriented Open-source Project and the Latest Major Release (v5.0) of the Core Package. *Astrophys. J.* **935**, 167. ([10.3847/1538-4357/ac7c74](https://doi.org/10.3847/1538-4357/ac7c74))